Mon. Not. R. Astron. Soc. **000**, 000–000 (0000) Printed 1 July 2014 (MN LATEX style file v2.2)

KIC 7582608: A new *Kepler* roAp star with frequency variability

Daniel L. Holdsworth[1⋆], B. Smalley[1], D. W. Kurtz[2], J. Southworth[1], M. S. Cunha[3], and K. I. Clubb[4]

[1]*Astrophysics Group, Keele University, Staffordshire, ST5 5BG, UK*
[2]*Jeremiah Horrocks Institute, University of Central Lancashire, Preston, PR1 2HE, UK*
[3]*Centro de Astrofisca e Faculdade de Ciências, Universidade do Porto, Rua das Estrelas 4150-762, Portugal*
[4]*Department of Astronomy, University of California, Berkeley, CA 94720-3411, USA*

arXiv:1406.7680v1 [astro-ph.SR] 30 Jun 2014

1 July 2014

ABSTRACT

We analyse the fifth roAp star reported in the *Kepler* field, KIC 7582608, discovered with the SuperWASP project. The object shows a high frequency pulsation at $181.7324\,\mathrm{d}^{-1}$ ($\mathrm{P} = 7.9\,\mathrm{min}$) with an amplitude of $1.45\,\mathrm{mmag}$, and low frequency rotational modulation corresponding to a period of $20.4339\,\mathrm{d}$ with an amplitude of $7.64\,\mathrm{mmag}$. Spectral analysis confirms the Ap nature of the target, with characteristic lines of Eu II, Nd III and Pr III present. The spectra are not greatly affected by broadening, which is consistent with the long rotational period found from photometry. From our spectral observations we derive a lower limit on the mean magnetic field modulus of $\langle B \rangle = 3.05 \pm 0.23\,\mathrm{kG}$. Long Cadence *Kepler* observations show a frequency quintuplet split by the rotational period of the star, typical for an oblique pulsator. We suggest the star is a quadrupole pulsator with a geometry such that $i \sim 66^\circ$ and $\beta \sim 33^\circ$. We detect frequency variations of the pulsation in both the WASP and *Kepler* data sets on many time scales. Linear, non-adiabatic stability modelling allows us to constrain a region on the HR diagram where the pulsations are unstable, an area consistent with observations.

Key words: asteroseismology – stars: chemically peculiar – stars: oscillations – stars: individual: KIC 7582608 – techniques: photometric.

1 INTRODUCTION

The rapidly oscillating Ap (roAp) stars can be found at the base of the classical instability strip on the Hertzsprung-Russell (HR) diagram, between the zero-age main-sequence and terminal-age main-sequence in luminosity. Since their first observation over 30 years ago (Kurtz 1982), about 60 stars of this type have been discovered. Most stars in this class have been discovered with ground-based photometric observations of known Ap stars. However, there are now some stars that have been detected through spectral line variations alone (e.g. Elkin et al. 2010, 2011; Kochukhov et al. 2013) and, with the launch of the *Kepler* satellite, high-precision space-based photometry (e.g. Balona et al. 2011b,a; Kurtz et al. 2011; Niemczura et al. 2014).

The roAp stars show pulsational periods in the range of 6 to 23 min with amplitudes in Johnson B of up to 10 mmag. These stars have their pulsational and magnetic axes inclined to the rotational axis, leading to the oblique pulsator model (Kurtz 1982; Bigot & Dziembowski 2002; Bigot & Kurtz 2011). Such an orientation allows the pulsation modes to be viewed from different aspects throughout the stellar rotational cycle.

The observations of roAp stars provide the best laboratory, beyond the Sun, to study the interactions between strong global magnetic fields, between $1 - 24\,\mathrm{kG}$, and stellar pulsations. Although pulsating in roughly the same frequency range, the driving mechanisms differ between the Sun and the roAp stars: the κ-mechanism acting on the hydrogen ionisation zone is thought to be the driving force of the roAp high-overtone pressure mode (p-mode) pulsations, although recent models by Cunha et al. (2013) suggest another excitation mechanism may be at work for a subset of roAp stars, whereas the solar pulsations are stochastically driven in the convection zone.

The Ap stars typically show strong over-abundances of rare-earth elements in their atmospheres of up to 10^6 times the solar value. Furthermore, these chemical anomalies often manifest themselves as spots on the stellar surface caused by atomic diffusion and trapping of ions by the strong magnetic field. These surface brightness anomalies are stable over many decades, allowing the rotation period of the star to be well determined.

To date there have been no roAp stars found in close binary systems. In fact, few Ap stars are in close binaries. There are, however, three candidates which are strongly suspected of being in visual binary systems (i.e. HR 3831, γ Equ and α Cir). Schöller et al. (2012) conducted a study of known roAp stars in the search for

⋆ E-mail:d.l.holdsworth@keele.ac.uk

companions using near-infrared imaging. They found six of their target roAp stars showed signs of companions, two of which were already known. However, from photometric data alone it is not possible to categorically determine whether the companions and the targets are gravitationally bound. Instead they calculate the probability of a chance projection, with their least certain companion having a chance projection probability of less than 2×10^{-3}. Regardless of whether they are gravitationally bound, the separation of visual binary stars means that stellar physics governing the individual stars is not effected. It is only in close binary systems that the components influence each other.

As previously mentioned, the *Kepler* mission has enabled the discovery of four roAp stars, all which have pulsation amplitudes much below the detection limits of ground-based photometry. The first to be found in the *Kepler* data was KIC 8677585 (Balona et al. 2011b), a known A5p star observed during the 10 d commissioning run with the 1 min short cadence (SC) mode. This roAp star pulsates at multiple frequencies in the range $125 - 145\,\mathrm{d}^{-1}$ with amplitudes in the range of $8.4 - 32.9\,\mu$mag. This star also shows a low frequency variation at about $3\,\mathrm{d}^{-1}$ which Balona et al. suggest is a g-mode γ Doradus pulsation, after consideration of other possibilities.

The second roAp star in the *Kepler* data is KIC 10483436 (Balona et al. 2011a) pulsating at two frequencies, each mode showing a quintuplet separated by the well determined rotation period. Again, the amplitudes of pulsation are much below the ground-based detection limits, namely in the range $5 - 69\,\mu$mag.

KIC 10195926 is the third identified roAp star in *Kepler* data (Kurtz et al. 2011). As with KIC 10483436, KIC 10195926 pulsates in two independent modes with amplitudes less than $170\,\mu$mag. Both modes show rotational splitting. The precision of the *Kepler* data has allowed the authors to claim KIC 10195926 has two pulsational axes, the first evidence of such a phenomenon in roAp stars.

The forth *Kepler* roAp is KIC 4768731 (Niemczura et al. 2014). Discovered through spectral classification, KIC 4768731 is the second slowest roAp pulsator, varying with a frequency of $61.45\,\mathrm{d}^{-1}$ at an amplitude of $62.6\,\mu$mag (Smalley et al., in preparation).

The fifth roAp star found in the *Kepler* field, which we analyse here, is KIC 7582608. Discovered using data from the SuperWASP project (Holdsworth et al. 2014, their 'J1844'), KIC 7582608 shows a single pulsation at $181.7324\,\mathrm{d}^{-1}$ with an amplitude of 1.45 mmag in the WASP broad-band filter ($4000 - 7000$ Å). The star was observed by the *Kepler* satellite for the full duration of the mission in the 30 min, Long Cadence (LC) mode. As a result, the true pulsation frequency is above the Nyquist frequency of the *Kepler* LC data. Although this results in a reduction of the observed pulsation amplitude, it has been shown that frequencies higher than the Nyquist can be reliably extracted from LC data (Murphy, Shibahashi & Kurtz 2013).

We present an analysis of spectral observations of KIC 7582608 which allows us to place the star on the theoretical HR diagram. We then show the WASP data used to initially detect the pulsations, and an in-depth study of the object with the *Kepler* data, followed by the results of linear, non-adiabatic modelling of the star.

2 SPECTROSCOPIC OBSERVATIONS

We have obtained two epochs of spectra for KIC 7582608 using the Hamilton Echelle Spectrograph (HamSpec) mounted on the 3.0-m Shane telescope at Lick Observatory (Vogt 1987). The observations were taken on 2012 July 24 and 2013 June 28 and have a resolution of $R \sim 37\,000$ and a signal-to-noise ratio (S/N) of about 40. The spectra were reduced in IDL with instrument specific software that performs flat-field corrections, de-biases, cosmic-ray cleaning, and wavelength calibrations. We co-added three spectra from 2012 and two from 2013 to produce two single spectra. Table 1 gives the spectral details, including the rotation phase at which the spectra were taken (see Section 4.1).

Table 1. Details of spectroscopic observations taken with HamSpec on the Shane 3.0-m telescope. The rotational phase has been calculated as shown in the text.

BJD-245 0000.0	Exposure time (s)	Rotational phase
6132.81003	1800	0.88
6132.83394	1800	0.88
6132.85516	1800	0.88
6471.79915	1800	0.47
6471.82036	1800	0.47

The two spectra show velocity shifts away from rest wavelengths for each epoch. These shifts are calculated by comparison with strong, unblended lines of Mg II 4481 Å, Ca II 4226 Å and the Na D lines, resulting in shifts of 45.8 ± 2.8 and $50.5 \pm 2.8\,\mathrm{km\,s}^{-1}$ for 2012 and 2013, respectively.

Figure 1 gives examples of spectral lines of elements found in the atmospheres of Ap stars extracted from our spectra. We note the variation of line strengths between the two different epochs and thus rotational phase. Close to maximum optical light, at phase 0.88 in 2012 (the upper black lines in Fig. 1), we see stronger lines of the rare earth elements compared to the second epoch at phase 0.47 (red lower lines in Fig. 1) where we observe the opposite hemisphere. The ephemeris for the phase (ϕ) calculations are calculated for the first light maximum (BJD) in the WASP data such that

$$\phi(E) = 245\,3151.8797 + 20\overset{\mathrm{d}}{.}4339 \times E \qquad (1)$$

where E is the number of cycles elapsed since the initial epoch.

The spectra show sharp lines indicative of a low $v \sin i$. We are unable to determine an accurate value of the $v \sin i$ from these spectra as we are limited by the spectral resolution, but we estimate $v \sin i \leqslant 4\,\mathrm{km\,s}^{-1}$. High resolution spectra are required to constrain this value.

The spectral lines typically used to determine the mean magnetic field modulus, $\langle B \rangle$, such as Cr II 6147.7 Å and Fe II 6147.7 and 6149.2 Å (Mathys 1990), show no sign of Zeeman splitting; however we attribute this to a lack of resolution in our spectra. Instead we use the method of Mathys & Lanz (1992) to estimate this value by comparing the relative intensities of the Fe II lines at 6147.7 and 6149.2 Å. There is a change of relative strengths between the two spectra, however the 6147.7 line remains the stronger of the two. We determine $\langle B \rangle = 3.13 \pm 0.32$ and 2.97 ± 0.32 kG for the 2012 and 2013 spectra, respectively. It is noted by Mathys & Lanz (1992) that for their stars with no resolvable magnetically split lines, this method of comparing Fe II 6147.7 and 6149.2 Å produces systematically lower values of the mean magnetic field modulus. We therefore suggest that the values derived here for KIC 7582608 are representative of a lower limit on $\langle B \rangle$.

We used UCLSYN (Smith & Dworetsky 1988; Smith 1992; Smalley, Smith & Dworetsky 2001) to determine the $\log g$ and $T_{\rm eff}$

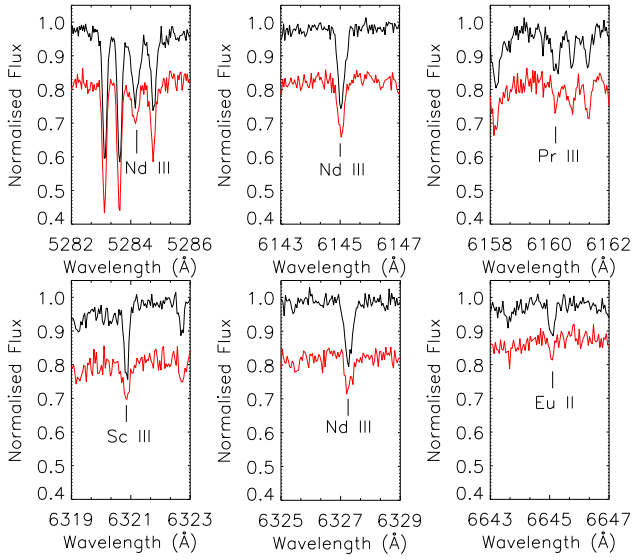

Figure 1. A selection of spectral lines which demonstrate the Ap nature of KIC 7582608. The upper black line shows the 2012 spectrum, with the lower red line showing the 2013 spectrum offset by 0.15 for clarity. There is clear variability in the strength of the peculiar lines due to the rotational phase variability. Both spectra have had velocity shifts removed to align the spectral lines with their rest wavelengths.

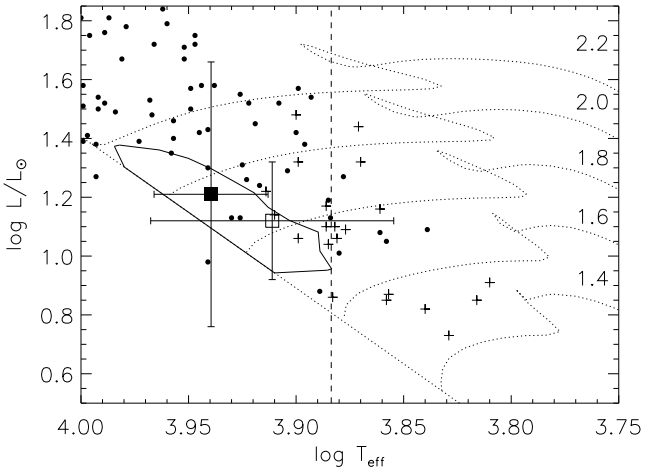

Figure 2. The position of KIC 7582608 in the theoretical HR diagram. The filled square is calculated with the temperature from the spectra and the derived radius, while the open square is calculated from the KIC values. The other roAp stars (crosses) and noAp stars (dots) are also shown for context. The vertical dashed line indicates the lower temperature tested for the models, and the area enclosed by the solid line represents the region where unstable modes are present at the observed frequency of $181.7324\,\mathrm{d}^{-1}$ (see Section 6 for further details). The zero-age main-sequence and evolutionary tracks are from Bertelli et al. (2008).

by performing an abundance analysis by measuring the equivalent widths of 77 Fe I lines and 57 Fe II lines. The effective temperature was found to be $T_{\rm eff} = 8700 \pm 100$ K by requiring no dependence of abundance with excitation potential. For the $\log g$ determination, we tested the ionisation balance between Fe I and Fe II. We found $\log g = 4.3 \pm 0.4$ (cgs). The photometrically derived value presented in the *Kepler* Input Catalogue (KIC) of 4.1 agrees with our calculation. These results were also confirmed by minimising the scatter in the measured abundances.

The Fe abundance measured from the 77 lines is $\log \mathrm{A(Fe)} = 8.4 \pm 0.2$, indicating an over-abundance relative to solar of $[\mathrm{Fe/H}] = +0.9$ dex based on the solar chemical composition presented by Asplund et al. (2009).

We have also determined the $T_{\rm eff}$ of KIC 7582608 using stellar spectral energy distribution (SED) fitting. We have used literature photometry from 2MASS (Skrutskie et al. 2006), U, B and V magnitudes from Everett, Howell & Kinemuchi (2012), g', r' and i' from Greiss et al. (2012), the TASS I magnitude (Droege et al. 2006), and GALEX fluxes (Martin et al. 2005) to reconstruct the SED. To determine the reddening of the star, we measured the Na D lines from our spectra and applied the relation of Munari & Zwitter (1997) to derive an $E(B-V) = 0.04 \pm 0.02$.

The stellar $T_{\rm eff}$ value was determined by fitting a [M/H] = 0.0 Kurucz (1993) model to the de-reddened SED. The model fluxes were convolved with photometric filter response functions. A weighted Levenberg-Marquardt non-linear least-squares fitting procedure was used to find the solution that minimised the difference between the observed and model fluxes. We used the $\log g = 4.3 \pm 0.4$ derived from the spectra for the fit. The uncertainty in $T_{\rm eff}$ includes the formal least-squares error and adopted uncertainties in $E(B-V)$ of ± 0.02, $\log g$ of ± 0.4 and [M/H] of ± 0.5 added in quadrature. As a result of the SED fitting, we derive a temperature of 8670 ± 450 K for KIC 7582608. Assuming a standard error of 200 K for the KIC temperature, their quoted value of 8149 ± 200 K agrees with our measurements.

3 POSITION IN THE HR DIAGRAM

To place KIC 7582608 in a theoretical HR diagram, we used both our calculated values from the spectra and adopted the values from the KIC. From the KIC, the values are $R = 1.82\,\mathrm{R}_\odot$, $T_{\rm eff} = 8149$ K, and $\log g = 4.10$. From these we calculate the star's luminosity, L, as $\log L/L_\odot = 1.12$.

Using the values derived from the spectra, namely $T_{\rm eff} = 8700 \pm 100$ K, $\log g = 4.3 \pm 0.4$ and [Fe/H]$= 0.9 \pm 0.5$, and the calibrations from Torres, Andersen & Giménez (2010), we derive the mass, radius and luminosity of KIC 7582608 of: $M = 2.37 \pm 0.43\,\mathrm{M}_\odot$, $R = 1.77 \pm 0.92\,\mathrm{R}_\odot$ and $\log L/L_\odot = 1.21 \pm 0.45$.

The positions of KIC 7582608 are shown in Fig. 2 along with other roAp stars and non-oscillating Ap (noAp) stars for which temperatures and luminosities are available in the literature. The position of the open square is determined from the KIC values, whilst the filled square is from spectral values. In both cases, KIC 7582608 appears to be close to the zero-age main-sequence, and is amongst the hotter, if not the hottest, known roAp stars. Further spectral observations are required to improve the effective temperature and luminosity measurements.

It is important to note here that both positions fall within the area bound by the solid lines. It is in this region that modelling has shown unstable pulsation modes of the same frequency as that observed in KIC 7582608. The modelling will be addressed in full in Section 6.

4 SUPERWASP DISCOVERY DATA

We present here the data which led to the identification of KIC 7582608 as a roAp star. We provide a short summary of the WASP instrument and data here and refer the reader to Pollacco et al. (2006) and Holdsworth et al. (2014) for details of the WASP project and the techniques used to identify KIC 7582608, respectively.

The SuperWASP instruments consist of eight 200 mm,

Table 2. Details of WASP observations of KIC 7582608. BJD is given as BJD−254 0000.0

WASP season	BJD start	Length (d)	Number of data points	χ^2/n
2004a	3139.67092	138.69311	1967	3.47
2004b	3139.66262	116.82519	1586	4.15
2004*	3139.66262	138.70141	3553	3.78
2007a	4230.56374	66.10058	3381	0.84
2007b	4297.39089	38.08300	1660	1.16
2007*	4230.56374	104.91015	5041	0.94
2008	4577.59791	112.95654	7585	10.04
2009	4941.57840	125.93750	10917	1.08
2010	5307.57254	124.95556	12293	1.00

*Combined data sets a and b.

$f/1.8$ Canon telephoto lenses backed by Andor CCDs of 2048×2048 pixels observing $\sim$61 deg^2 each through broadband filters covering a wavelength range of $4000 - 7000$ Å. This set-up enables simultaneous observations of up to 8 fields with a pixel size of 13.7 arcsec. The instruments capture two consecutive 30 s integrations at a given pointing, then move to the next observable field. Typically, fields are revisited every 10 min. The data pass through a reduction pipeline correcting for primary and secondary extinction, the colour response of the instrument and the zero-point. The data are also corrected for instrumental systematics with the SysRem algorithm of Tamuz, Mazeh & Zucker (2005). Individual stellar magnitudes are extracted based on positions from the USNO-B1.0 catalogue (Monet et al. 2003) down to a limit of about magnitude 15.

KIC 7582608 was initially observed by WASP in 2004, and subsequently in 2007, 2008, 2009 and 2010, denoted as 'seasons' (there are multiple observing blocks per year if the target appears in more than one observing field, in this case denoted a and b in Table 2). Observations are taken in a variety of conditions that can result in significant errors and night to night fluctuations in the final data. Table 2 details the WASP observations of KIC 7582608, with the final column representing the weighted reduced-χ^2 (Bevington 1969) which aims to characterise the data using the number of points and scatter in the light curve such that

$$\chi^2/n = \frac{\Sigma((\mathrm{mag} - \mathrm{median(mag)})/\sigma)^2}{(n-1)}. \quad (2)$$

As can be seen from Table 2, the 2004 and, especially, the 2008 seasons of data have a χ^2/n value deviating from the desired value of 1.00 indicating that these seasons may result in less reliable results.

4.1 The rotation signature

The WASP light curve for KIC 7582608 shows the strong modulation which is typical of Ap stars. We calculated a Lomb-Scargle periodogram using the Fortran code FASPER (Press & Rybicki 1989; Press et al. 1992) in the frequency range $0 - 2\,\mathrm{d}^{-1}$. We used the best quality data for the calculation spanning 1201.9644 d to best constrain the period, i.e. the 2007, 2009 and 2010 seasons. Using PERIOD04 (Lenz & Breger 2005), we found a rotation frequency of $\nu_{\mathrm{rot}} = 0.0489\,382 \pm 0.000\,004\,\mathrm{d}^{-1}$, which corresponds to a rotation period of $P_{\mathrm{rot}} = 20.4339 \pm 0.0017$ d. The errors are the analytical errors taken from PERIOD04 (Montgomery & Odonoghue 1999). Fig. 3 shows a labelled periodogram and phase folded light curve of just the 2010 season for clarity. As well as the rotation frequency we detect a second weaker signature at $2\nu_{\mathrm{rot}}$. In the bottom panel of Fig. 3 this can be seen as a small bump at phase 0.5. This signature can be explained with another spot on the opposite hemisphere of the star which appears smaller, most likely due to projection effects.

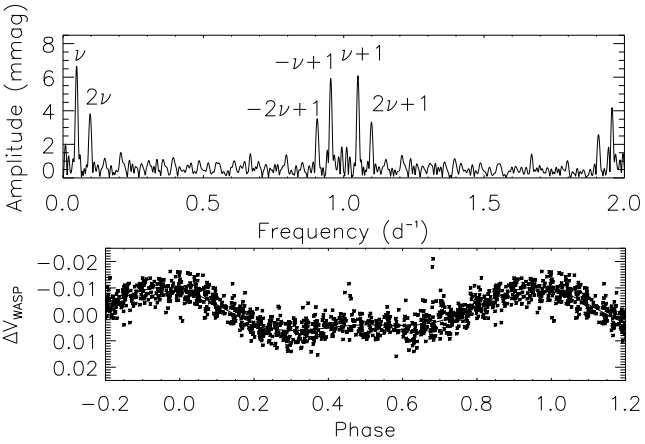

Figure 3. Top panel: labelled periodogram of the 2010 season of WASP data, where ν_{rot} is the rotation frequency. Bottom panel: the phase folded light curve of the 2010 WASP data. The data are folded on the period derived from combining the 2007, 2009 and 2010 seasons, i.e. 20.4339 d and are shown in phase bins of 10 : 1.

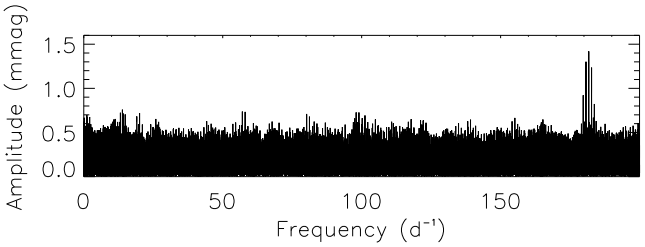

Figure 4. Periodogram of the 2010 season WASP data after pre-whitening has occurred. The pulsation is clearly seen at $181.7324\,\mathrm{d}^{-1}$ at an amplitude of about 1.45 mmag.

4.2 The pulsation signature

To best analyse the pulsation in the WASP data, we pre-whitened the data to $10\,\mathrm{d}^{-1}$ by fitting a series of sinusoids to a limit of the approximate noise level at high-frequency for each data set individually. The noise level varied greatly between seasons, with pre-whitening occurring between 0.7 and 2.5 mmag for the flattest and most noisy data sets, respectively. In this way we removed the rotational variability from the light curve, and any further systematic effects, especially the dominant 'red' noise (Smith et al. 2006) remaining after the data have passed through the WASP pipeline. The resulting periodogram for the 2010 season is shown in Fig. 4. The results of a non-linear least-squares fit is shown for each season in Table 3.

Other than extracting the correct pulsational frequency and amplitude (in the WASP photometric pass-band), there is no further information that can be gleaned from the WASP data. As previously mentioned, the pulsation frequency is above the Nyquist frequency of *Kepler* LC data and some confusion may be had in disentangling the true peak from the many other aliases if the data do not have a large enough time span, a scenario which the WASP data allows

Table 3. Frequencies, amplitudes and phases of the pulsation extracted from the WASP data using a non-linear least-squares fit. The zero-point for the phases is BJD 245 3151.6245.

Season	Frequency (d^{-1})	Amplitude (mmag)	Phase (rad)
2004a	181.7247 ± 0.0011	1.429 ± 0.337	1.644 ± 0.238
2004b	181.7243 ± 0.0017	1.444 ± 0.435	1.865 ± 0.307
2004	181.7241 ± 0.0013	1.274 ± 0.316	1.827 ± 0.252
2007a	181.7339 ± 0.0008	1.452 ± 0.222	-1.386 ± 0.152
2007b	181.7353 ± 0.0009	1.638 ± 0.373	1.577 ± 0.228
2007	181.7347 ± 0.0006	1.549 ± 0.195	-0.769 ± 0.125
2008	181.7334 ± 0.0011	1.597 ± 0.349	1.465 ± 0.220
2009	181.7387 ± 0.0004	1.460 ± 0.154	0.724 ± 0.105
2010	181.7276 ± 0.0005	1.436 ± 0.158	2.067 ± 0.109

us to disregard. The noise characteristics of the WASP data do not allow for a reliable extraction of rotational sidelobes as they occur at approximately the same amplitude. We do however notice that the frequencies of the different seasons vary beyond their errors, an observation we shall revisit in Section 5.3.

5 *KEPLER* OBSERVATIONS

As previously mentioned, KIC 7582608 has been observed by the *Kepler* satellite for the full duration of the mission, a little over 4 y. The data were collected in the LC mode with a cadence of 30 min. There are no SC data for this target.

5.1 The rotation signature

Fig. 5 shows Q10 of the data. It is clear that the star has a well defined rotation period, mapped out by surface brightness anomalies in two hemispheres. This is typical behaviour of an Ap star which has a strong global magnetic field. To determine the rotation period of the star, we combined all quarters of data, removing any obvious outlying data points and quarter-to-quarter zero-points resulting in a light curve varying about zero magnitude. We then calculated a periodogram which showed two frequencies, the rotation frequency and the harmonic. The principal peak has a frequency of $\nu_{\rm rot} = 0.0488\,920 \pm 0.0000\,003\,{\rm d}^{-1}$, which corresponds to a rotation period of $P_{\rm rot} = 20.4532 \pm 0.0001$ d. As with the WASP data, the rotational frequency was calculated with PERIOD04, and the errors are the analytical errors. This value is close to that derived from the WASP light curve in Section 4.1, but deviates by ~ 28 min. The *Kepler* data have a much higher duty cycle than that of the WASP observations, so the daily and seasonal gaps in the WASP data have led to the discrepancies between the two derived rotation periods. Combining the two data sets provides a time string covering 3285 d from which we calculate a rotation period of $P_{\rm rot} = 20.4401 \pm 0.0005$ d.

5.2 The pulsation signature

Due to the barycentric corrections applied to the time stamps of the *Kepler* observations, the regular sampling of the data has been broken. Murphy, Shibahashi & Kurtz (2013) have shown that it is possible to directly analyse the true pulsation frequency even if it occurs above the nominal Nyquist frequency of the LC data, rather than analysing a low-frequency alias. This is the case of the pulsation in KIC 7582608.

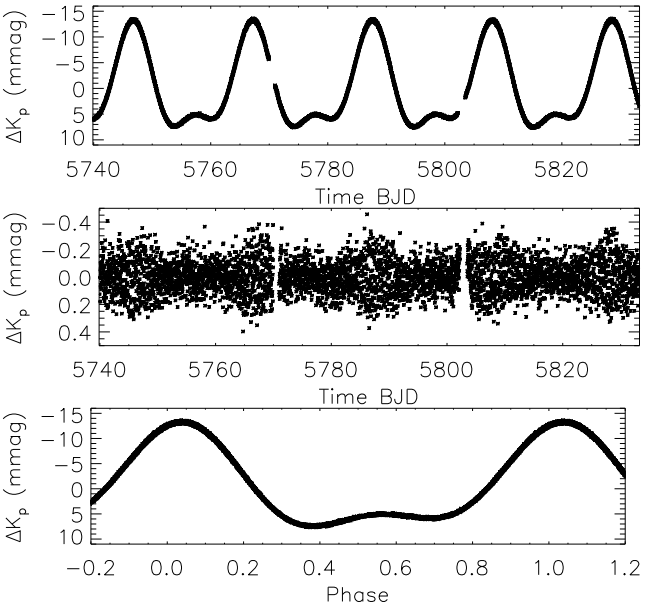

Figure 5. Top panel: The LC data of KIC 7582608 from Q10. The ordinate is BJD-245 0000. Middle panel: Q10 LC data after high-pass filtering (described in Section 5.2) has removed the rotational modulation signature leaving only the pulsation variation. Only the pulsation envelope is seen here due to the scale. Note that the pulsation maxima coincide with the rotational maxima. Bottom panel: The phase folded light curve.

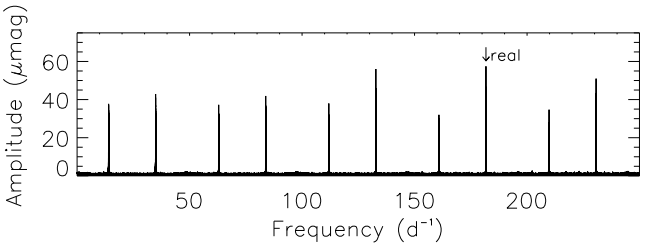

Figure 6. Periodogram of the individually pre-whitened Q00−Q17 *Kepler* data. The real peak can be identified as the strongest signal.

To analyse the high frequency signature, we pre-whiten each quarter of data to the approximate noise level at higher frequencies, thus we remove all peaks with amplitudes greater than 5 μmag below 1 d^{-1}. This procedure removes both instrumental variations at very low frequency, and the rotational spot variations. As these are well-separated in frequency from the 181 d^{-1} pulsation frequency, the filtering has no effect on our analysis, except to make the noise close to white noise so that the light curve can be examined by eye and so that the least-squares error estimates are realistic (i.e., are not influenced by the low-frequency variations). We initially combined the pre-whitened data and calculated a full periodogram to show the true pulsation in the LC data. Fig. 6 presents the result, with the highest amplitude peak at $181.7324\,{\rm d}^{-1}$, which agrees with that found from the WASP data in Section 4.2. Note that the amplitude is much lower than that seen in the WASP data as a result of the multiple Nyquist crosses.

Taking the full data set and extracting just the pulsation range shows, in Fig. 7, a "ragged" multiplet split by the rotation frequency of the star. The central peak is the true pulsation frequency, as confirmed with the WASP data, with the rotationally split side lobes

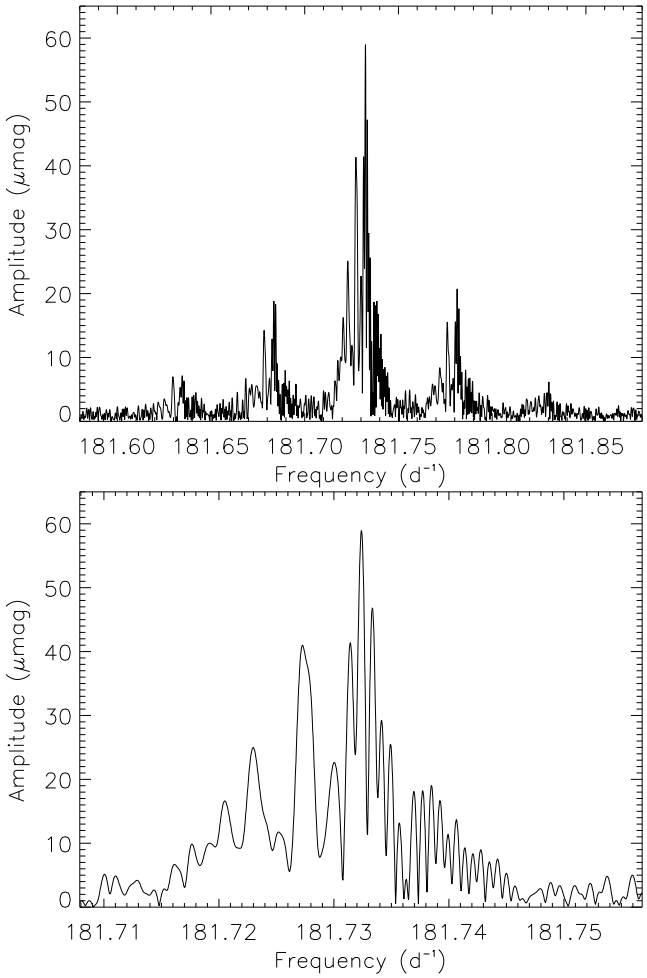

Figure 7. The roAp pulsation frequency seen in the *Kepler* Q00 − 17 LC data. Top: An amplitude spectrum showing the multiplicity of closely spaced peak around each of the frequency quintuplet components of the obliquely pulsating mode. Bottom: a higher resolution look at the central peak of the quintuplet. Each of the rotational sidelobes has a similar structure, as expected for oblique pulsation.

describing the variations in phase and amplitude with the varying aspect over the rotation cycle. A closer look at the principal peak, Fig. 7 bottom, highlights the complex and unstable nature of the pulsation frequency, an observation we address in Section 5.3.

We have analysed each quarter individually, with the periodograms shown in Fig. 8 and the results of a linear least-squares fit shown in Table A1. To produce the data in Table A1, we found the highest amplitude peak in the range $181 - 182\,\mathrm{d}^{-1}$ and removed it with a linear least-squares fit. The residuals were then searched for the next highest peak, which was removed in the same way. When we had removed the pulsation signatures from the light curve, we then forced the sidelobes to be separated by exactly the rotation frequency to test the phase relations of the sidelobes in the original data. We find that $\phi_{-1} = \phi_{+1} \neq \phi_0$ suggesting that the mode is a distorted mode.

To test this result, we assume a basic geometry of a pure dipole mode with sidelobes resulting from distortion and rotation alone. In this case, $l = 1$ and $m = 0$. We use the relationship of Kurtz, Shibahashi & Goode (1990) between the amplitude of the central peak and the first sidelobes such as

$$\tan i \tan \beta = \frac{A_{+1} + A_{-1}}{A_0}, \tag{3}$$

where i is the rotational inclination of the star, β is the obliquity of the pulsation axis to the rotation axis, and A_0 and $A_{\pm 1}$ are the amplitudes of the central and first sidelobes, respectively. Using an average value for the the amplitudes calculated for each quarter of data (Table A1), we calculate $\tan i \tan \beta = 0.67 \pm 0.03$. This provides us with a relation between i and β, but not the values individually. For this we require a measure of the $v \sin i$ of the star, and an estimate of the stellar radius. We are unable to measure the $v \sin i$ in Section 2, however we are able to provide an upper limit of $4\,\mathrm{km\,s^{-1}}$. Using this upper limit, the radius derived from the Torres, Andersen & Giménez (2010) relationships of of $1.77\,\mathrm{R}_\odot$, and the rotation period of $20.4339\,\mathrm{d}$, we can estimate a limit on i of $\sim 66^\circ$ and on β of $\sim 17^\circ$. From the double wave nature of the light curve shown in Fig. 5, it is apparent that $i + \beta > 90^\circ$ so that both magnetic poles are seen, a criterion that our calculated values do not fulfil. In fact, no values of i and β sum to $> 90^\circ$ and satisfy $\tan i \tan \beta = 0.67$. We therefore calculate $\tan i \tan \beta$ using the assumption that the pulsation is a quadrupole mode such that $l = 2$ and $m = 0$. Again, from Kurtz, Shibahashi & Goode (1990), we have the relationship between the combined relative amplitudes of the first and second sidelobes which can be used to describe the geometry of the pulsation such as

$$\tan i \tan \beta = 4 \times \frac{A^{(2)}_{+2} + A^{(2)}_{-2}}{A^{(2)}_{+1} + A^{(2)}_{-1}}, \tag{4}$$

where i and β are as before, and $A^{(2)}_{\pm 1}$ and $A^{(2)}_{\pm 2}$ are the amplitudes of the first and second sidelobes of the quadrupole mode, respectively. Using an average value for the the amplitudes calculated for each quarter of data (Table A1), we calculate $\tan i \tan \beta = 1.44 \pm 0.14$. Taking the value of i as before, we calculate β to be $\sim 33^\circ$ resulting in $i + \beta > 90^\circ$. Such a result suggests that KIC 7582608 is a quadrupole pulsator.

5.3 Pulsation variability

Some roAp stars show highly stable pulsational frequencies, amplitudes and phases over time spans of years. Others have variable frequencies. Kurtz et al. (1994) and Kurtz et al. (1997) discussed frequency variability for the roAp star HR 3831 with ground-based data spanning 16 y, albeit with large gaps through the years. While they originally suggested that the frequency variability could be cyclic, that was not supported by the later work. Similar frequency variability was reported for another roAp star; Martinez, Kurtz & van Wyk (1994) discuss HD 12932 and point out seven further roAp stars for which frequency variability was known at that time.

The question arises as to what causes frequency variability in roAp stars. Is it a change in the pulsation cavity, either because of structural changes in the star, or changes in the magnetic field? Is it externally caused by orbital perturbations of a companion, or companions? Is it some combination of these?

Balona (2013) shows an amplitude spectrum for KIC 10483436 where the largest amplitude pulsation mode has a frequency quintuplet, split by the rotation frequency ($P_{\mathrm{rot}} = 4.3\,\mathrm{d}$) , caused by oblique pulsation. For the entire *Kepler* data set the amplitude spectrum can be described as "ragged"; that is, the peaks of the quintuplet are composed of many closely spaced peaks in the amplitude spectrum. This is similar in nature to our Fig. 7. While this is typical for stochastically excited pulsators,

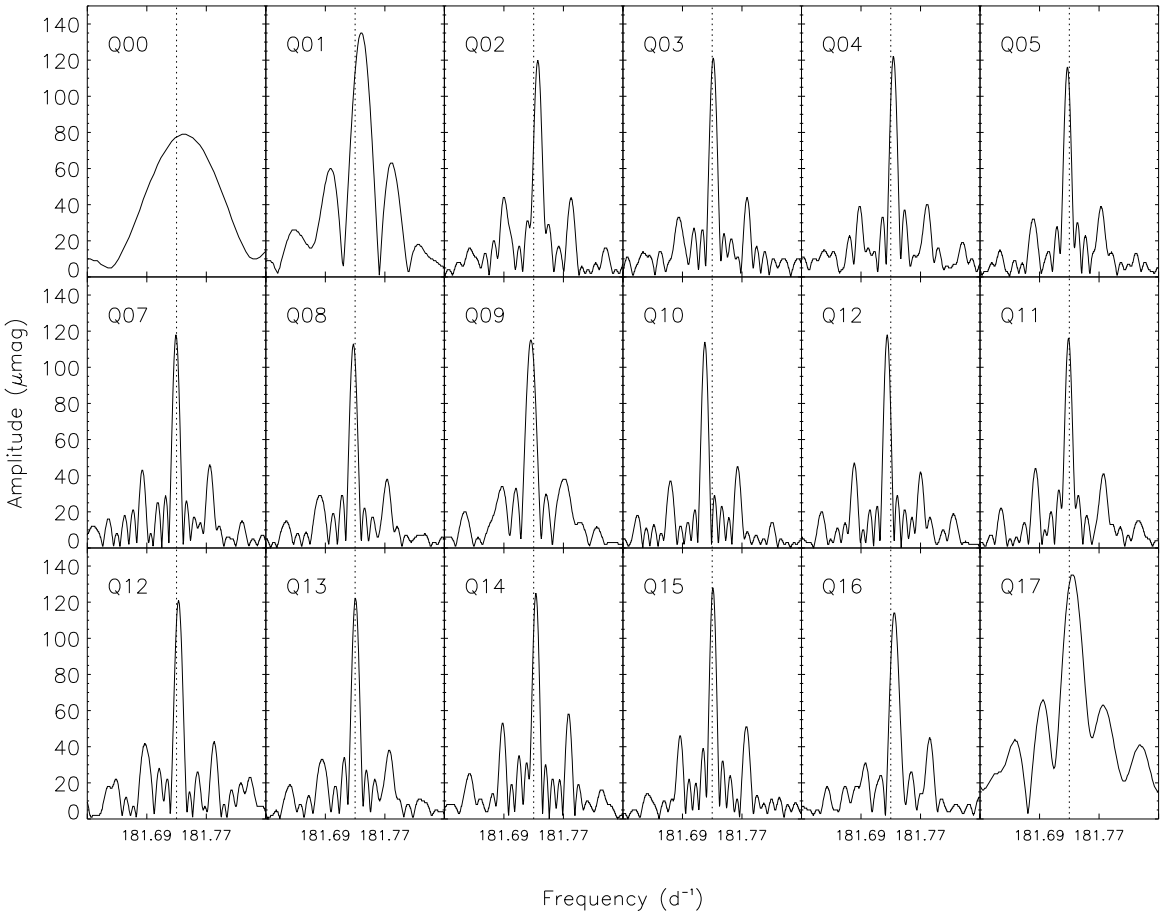

Figure 8. Periodograms of each quarter of *Kepler* data centred on the pulsation frequency. The vertical dashed line at 181.73 d^{-1} is to guide the eye when noting the frequency variability from quarter to quarter, as discussed in Section 5.3. The values of the pulsation frequency are shown in Table A1.

such as solar-like stars and red giant stars, stochastic excitation is not likely for roAp stars. Thus the multiplicity of closely spaced peaks that make up each component of the oblique pulsator quintuplet must arise because of frequency, amplitude and/or phase variations over the time span of the data set.

Given the history of non-periodic frequency modulation seen in some roAp stars, we therefore need to study the time dependence of both the frequency of the pulsation mode in KIC 7582608 and its amplitude. To do this, we used the same data set as in Section 5.2, but split the data into sections with a length of 100 pulsations cycles, or about 0.55 d. We then fitted $\nu_1 = 181.7324\,\mathrm{d}^{-1}$, which is the highest peak in Fig. 7, by linear least-squares to each section of the data, giving 2487 measurements. The function fitted was

$$\Delta m = A\cos(\nu(t - t_0) + \phi)\,. \quad (5)$$

If the pulsation mode is stable, then we expect to see amplitude and phase modulation only with the rotation frequency 0.0489 382 d^{-1} determined in Section 4.1 as expected in the oblique pulsator model.

5.3.1 *Amplitude modulation*

Fig. 9 shows the pulsation amplitude as a function of rotational phase for the entire 1460 d data set. The measurements have been averaged in groups of 20 within narrow phase bins to smooth the curve. It can be seen that there is no change in pulsation amplitude over the entire 1460 d time span of the data. The only variation seen is the amplitude modulation with rotation caused by the oblique pulsation mode.

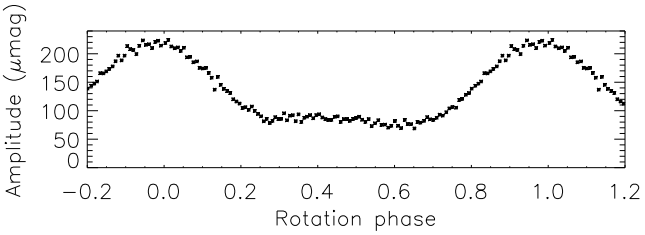

Figure 9. Pulsation amplitude as a function of the 20.4339 d rotation phase, calculated with all quarters of data. The zero point in time, t_0 = BJD 2453151.8797, was selected to be the time of maximum rotational brightness of KIC 7582608, hence we see that maximum pulsation amplitude coincides with the rotational light extremum.

This variation is similar to that of another *Kepler* roAp star, KIC 10195926. Figure 10 of Kurtz et al. (2011) shows the double wave nature of the amplitude variation with rotation phase, caused by the geometry of the mode and differing aspects of our view. This is also the case here in KIC 7582608 seen in Fig. 5 which suggests

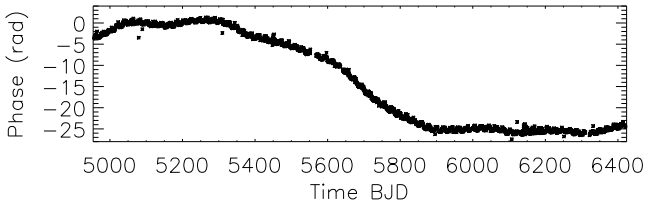

Figure 10. The phase variation over the entire observation period. A constant pulsation frequency would led to a straight line in the plot, the variation seen suggest there is a better frequency fit to the data. To form a continuous plot we have added or subtracted 2π rad to the phase where appropriate.

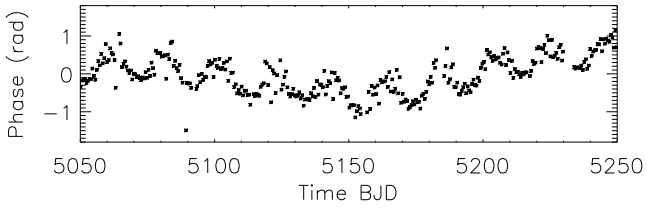

Figure 11. This plot shows the phases determined for a section of the 0.55 d long (100 pulsation cycles) in the time span JD $2455048 - 2455250$.

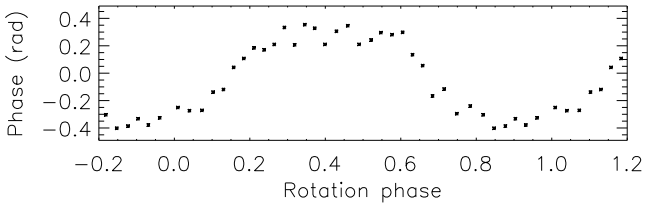

Figure 12. This plot shows the phases determined for a section of the 0.55 d long (100 pulsation cycles) in the time span JD $2455048 - 2455250$. The points are 10-point averages of the 0.55 d phases in narrow rotational phase bins for smoothing.

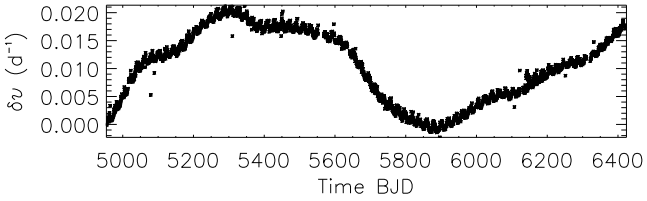

Figure 13. The frequency variability, $\delta\nu(t)$, over the 1460 d data set calculated from Fig. 10 with a linear trend removed and equation (9).

that both poles may be seen in this star, although with low visibility for the second pole (the small bump seen in Fig. 5 at rotation phase 0.5).

5.3.2 Phase and frequency variability

Unlike the amplitude, the phase varies dramatically over the 4 y time span. Fig. 10 shows the pulsation phase over the entire 1460 d data set from the same data used for the amplitudes. This is very different from the example of KIC 10195926 where the pulsation phase is stable over the entire observation period, and shows π-rad phase reversal at quadrature (figure 10. of Kurtz et al. (2011)). Selecting a shorter data range of 200 d, it is possible to see in Fig. 11 that the pulsation phase varies a with rotation phase, as is expected from the oblique pulsator model.

To examine the rotational variation of the pulsation phase, we have removed the longer term curvature in Fig. 11 and phased the data with the rotation period as seen in Fig. 12. The pulsation phase varies by nearly 1 rad over the rotation cycle. This is similar to what is seen in other roAp stars that have been studied in enough detail. The best cases to refer to are those of KIC 10195926 (Kurtz et al. 2011), HR 3831 (Kurtz et al. 1997) and HD 6532 (Kurtz et al. 1996). For those three stars both pulsation poles are seen, the principal pulsation modes are primarily dipolar, and there is an obvious phase reversal at quadrature. However, outside of that phase reversal, there is smooth pulsation phase variation over the rotation period with an amplitude of order of 1 rad, just as in KIC 7582608. Therefore, the only difference for KIC 7582608 is that the other pulsation pole does not come into sight. This variation of pulsation phase with rotation is a consequence of magnetic and rotational effects on the light curve, along with the geometry of the mode and aspect of our view (Bigot & Kurtz 2011).

In equation (5) it can be seen that phase and frequency are coupled; a change in one could be interpreted as a change in the other. If we assume that we have a constant phase and only frequency variability, then we may write the light variations as

$$\Delta m = A\cos(\nu(t)(t-t_0)+\phi_0)\,, \tag{6}$$

where

$$\nu(t) = \nu_0 + \delta\nu(t) \tag{7}$$

and ν_0 is constant. It is then easy to regroup the terms to give

$$\Delta m = A\cos(\nu_0(t-t_0)+\phi(t))\,, \tag{8}$$

where

$$\phi(t) = \phi_0 + \delta\nu(t)\,(t-t_0)\,. \tag{9}$$

Hence, frequency and phase variability are inextricably intertwined. We therefore interpret the phase variations to be the result of frequency variability.

Fig. 10 is the equivalent of a traditional $O-C$ diagram. With a correct constant frequency we expect the phases to follow a straight line in the plot, any linear trend with a slope can mean that another frequency is a better fit. Equations $6-9$ allow an easy conversion of phase to frequency. Anywhere in Fig. 10 where the trend is non-linear, frequency variations are present.

From the deviations of linearity in Fig. 10, it is possible to see that the pulsation frequency of KIC 7582608 is strongly variable over the 1460 d data set. That is the reason for the "raggedness" in the amplitude spectrum seen in Fig. 7.

To examine the frequency variability further, we removed a linear trend from the phases in Fig. 10 – which is equivalent to fitting a different starting frequency initially – and converted the phases to frequency changes using equation (9). The result is shown in Fig. 13. It can be seen that there is frequency variability on many time scales. Whether the largest variation seen on the length of the data set is a consequence of a binary companion or is intrinsic is uncertain, but clearly much of the frequency variability must be intrinsic to be on so many time scales. This does show why the amplitude spectrum is "ragged", although the origin of the frequency variability is not clear.

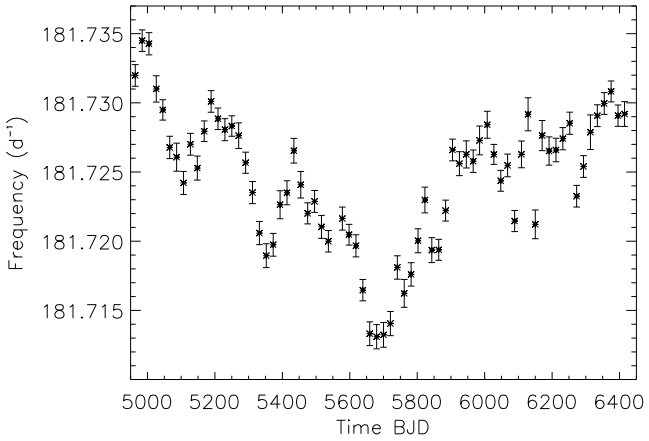

Figure 14. Frequencies calculated for each rotation period using a non-linear least-squares routine.

5.3.3 Binary interpretation of frequency variation

One potential cause of frequency variability is external. If the pulsating star is a member of a binary, or multiple system, then the orbital motion causes frequency variability as a result of the Doppler shifts. This is a periodic phenomenon and has been described in detail by Shibahashi & Kurtz (2012), who show that the orbital motion results in each pulsation frequency peak being split into a multiplet separated by the orbital frequency. They call their technique for studying binary motion FM, for frequency modulation. The number of components to the multiplet is a function of a parameter α, which itself is dependant on the mass of the companion, the orbital period, the pulsation period and the eccentricity; in general, for low eccentricity and low α only a triplet is expected. Fig. 7 is not reminiscent of such a simple pattern. Periodic amplitude modulation also produces frequency multiplets in the amplitude spectrum; oblique pulsation is a good example of this. Again, Fig. 7 is not reminiscent of periodic amplitude modulation.

It is evident that in KIC 7582608 there are frequency variations occurring over many different time scales. As such, Fig. 7 does not fit a simple FM pattern. However, due to the possibility that the large scale frequency variations are due to binary interaction, it is important to investigate this further as, if confirmed, this is an important result for roAp binary systems. To pursue this line of enquiry, we split the pre-whitened Q00 − 17 data into sections of $P_{\rm rot}$ in length, giving 72 individual data sets to analyse. In doing this, we aim to reduce the effects of the shorter time-scale frequency variations which we have shown to be present. This provides us with good temporal coverage of a binary orbit without sacrificing frequency resolution. A periodogram for each rotation cycle was then calculated and fitted with a non-linear least-squares routine to extract the pulsation frequency and corresponding error. In doing this, we extract just the pure frequency variations, allowing the phase to be a free parameter in the fitting procedure. Each individual data set is analysed independently, such that the phases extracted are not of use here. This, therefore, is a different analysis to that presented in Figs. 10 and 13, where we concentrate on phase rather then frequency variations. The results of this analysis are presented in Fig. 14 and Table A2. It is clear that there are long term frequency variations on approximately the same time period as the observations. The extent of the frequency variations is about $0.02\,{\rm d}^{-1}$ (0.25μHz).

Assuming that the frequency variability is due to an external factor, i.e. due to orbital motion, it is possible to extract orbital parameters from the frequency variations. Taking the frequency shifts to be caused by Doppler shifts, the frequencies can be converted into radial velocities (RVs) using:

$$V_{\rm rad} = c\left(\frac{\nu_i - \nu_{\rm ref}}{\nu_{\rm ref}}\right), \tag{10}$$

where c is the speed of light, ν_i is a given frequency and $\nu_{\rm ref}$ is a reference frequency. As we do not know the intrinsic pulsation frequency, we adopt here $\nu_{\rm ref}$ to be the mean of ν, resulting in relative, rather than absolute, radial velocities. In addition to the *Kepler* data, we have included the frequencies of each WASP season of data from Table 3, adding a further nine data points, now totalling 81, from which to calculate the binary parameters (Table A3).

To determine the orbital parameters, we pass our RV measurements to JKTEBOP (Southworth 2013), testing both circular and eccentric orbits. The best fit the code produces is that of an eccentric system, with an eccentricity of $e = 0.39$ and a period of $P_{\rm orb} = 1203 \pm 34$ d. We have folded the data on the given period and plotted the resultant fit, as shown in Fig. 15. The full parameters are shown in Table 4. To determine the absolute values for the RVs, we have included two spectroscopically determined RVs (blue dots in Fig. 15) from the Lick spectra reported in Section 2. It must be noted that the spectroscopic RVs are not used in determining the fit, just the absolute values.

The fit is in good agreement with most of the *Kepler* and WASP observations. The 2007 and 2008 seasons of the WASP data (between BJD 4200 and 4700 in Fig. 15 left) are perhaps the worst fitting data. The 2008 data are of low quality (see Table 2) which may explain the discrepancy. However, we cannot explain the misfitting 2007 data, which are of good quality.

Using the mass function presented in Table 4, we calculate a set of solutions for the secondary mass given a range of binary inclination angles. The results are presented in Table 5. It is likely that the inclination is close to 90° as we detect no signature from a secondary star in the spectra presented in Section 2, implying a significant luminosity difference.

It is clear that KIC 7582608 is in need of long-term follow-

Table 4. Radial velocity fit parameters for KIC 7582608. The mass function was calculated assuming a value of m_1 of $1.8\,{\rm M}_\odot$.

Parameter	Value
$e\cos\omega$	-0.301 ± 0.089
$e\sin\omega$	-0.247 ± 0.088
e	0.390 ± 0.055
ω ($^\circ$)	219.3 ± 20.5
$P_{\rm orb}$ (d)	1203 ± 34
K_1 (km s^{-1})	10.62 ± 1.13
$f(m_1, m_2, \sin i)$ (M$_\odot$)	0.149 ± 0.016

Table 5. Calculated secondary masses for a given value of the binary inclination.

Inclination i ($^\circ$)	Secondary mass (M$_\odot$)
90	1.07
80	1.09
70	1.16
60	1.30
50	1.55
40	2.00

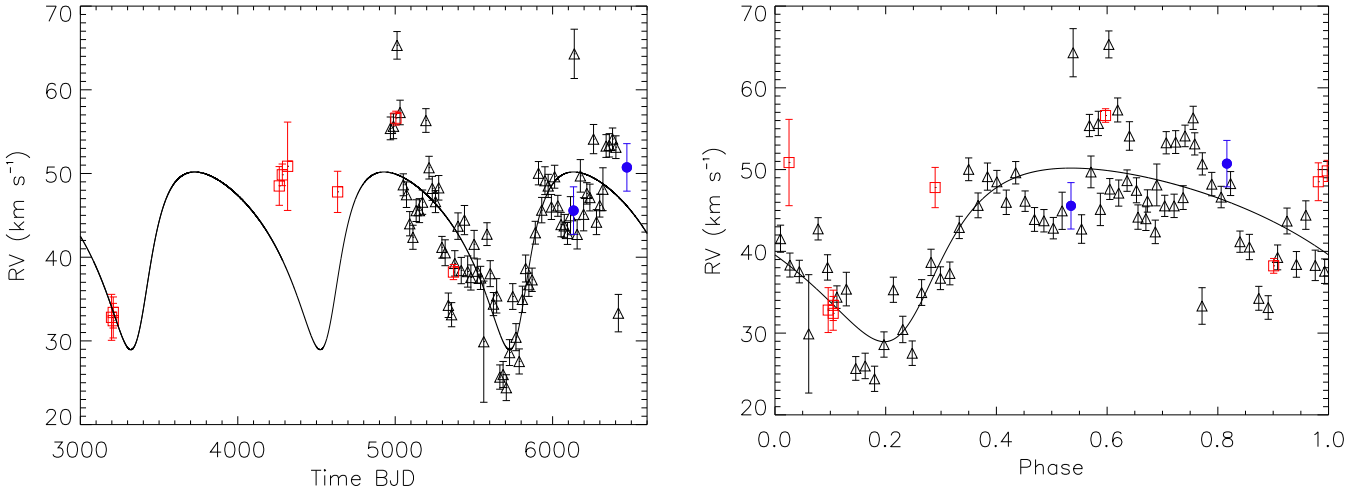

Figure 15. The phase folded eccentric radial velocity curve derived for KIC 7582608 from photometric data. The black triangles are *Kepler* data, the red squares represent WASP data, and the blue dots are derived from the spectra. The line represents the fit from JKTEBOP. The spectroscopic RVs were not used to determine the fit, but used to determine the absolute value. The fit parameters are shown in Table 4.

up spectroscopic observations to further monitor the potential RV shifts.

6 MODELLING

The detection of even a single pulsation frequency in KIC 7582608 may provide additional constraints to the star's global properties. To investigate this possibility we carried out a linear, non-adiabatic stability analysis of a grid of models covering the theoretical instability strip for roAp stars (Cunha 2002), restricting the effective temperature to values larger than 7650 K, taken in intervals of 50 K. The grid comprises stellar masses between 1.7 $M_\odot$ and 2.2 $M_\odot$, varying in intervals of 0.05 $M_\odot$. The starting point for the grid is a set of evolutionary tracks computed with the code MESA (Paxton et al. 2011, 2013), with initial mass fraction of hydrogen and helium of $X = 0.70$ and $Y = 0.28$, respectively. The effective temperature and luminosities taken from these evolutionary tracks are then used to generate the equilibrium models necessary for the non-adiabatic computations. The analysis follows closely that first presented by Balmforth et al. (2001) and, with some additions, by Cunha et al. (2013). An important aspect of the models is that they are composed of two different regions, namely, the equatorial region, where convection proceeds normally, and the polar region, where convection is assumed to be suppressed by the magnetic field. We refer the reader to the works mentioned above for a detailed description of the models and corresponding physical assumptions.

Following Cunha et al. (2013), we have considered, for each set of mass, effective temperature, and luminosity, four different cases, which together cover the main uncertainties in the modelling. The first of these constitutes the standard case, in which the equilibrium model is characterised by the surface helium abundance $Y_{\rm sur} = 0.01$ and the minimum optical depth $\tau_{\rm min} = 3.5 \times 10^{-5}$, and the pulsation analysis applies a fully reflective boundary condition at the surface. The other four cases are obtained by swapping these properties, one at the time to: $Y_{\rm sur} = 0.1$, $\tau_{\rm min} = 3.5 \times 10^{-4}$, and a transmissive boundary condition.

Fig. 16 shows an example of the results obtained from the stability analysis for a fixed mass, effective temperature and luminosity. All four cases are shown for the polar region. For the equatorial region, the results of the different cases are very similar and, thus, we present only the standard case. Clearly, the growth rates are negative for all high radial order modes in the equatorial region, indicating pulsation stability when convection takes place normally. This is the usual situation for stars in this region of the HR diagram. In contrast, when convection is suppressed modes at the observed frequency become unstable in three out of the four cases studied for this set of mass, effective temperature and luminosity.

The results of the stability analysis performed on our grid are presented in Fig. 2. The enclosed region corresponds to the models that show unstable modes at the observed frequency in the polar region of at least one of the four cases studied. Despite the rather weak constraints that exist on the effective temperature and luminosity of KIC 7582608, there is a clear indication that the results of the stability analysis are consistent with the KIC values, as well as with the effective temperature determinations performed in this work. Thus, KIC 7582608 seems to be an additional example of the group of stars whose pulsational instability is well explained by the opacity mechanism acting on the hydrogen ionisation region. We note that this is in contrast with a number of cases discussed by Cunha et al. (2013), in which clear evidence exists for a disagreement between the observed frequency range and the region of frequencies predicted to be excited by this mechanism, and which led the authors to suggest that an alternative excitation mechanism, possibly connected to the perturbation to the turbulent pressure, must be in place for a subset of roAp stars.

Under the assumption that the opacity mechanism acting in the hydrogen ionisation region is indeed responsible for driving the observed frequency, the results of the stability analysis further constrain the possible values of the luminosity of KIC 7582608 as a function of its effective temperature. An improvement in the determination of the effective temperature and $\log g$ of this star in the future will, thus, lead to a stronger constraint on its luminosity, via the results of the stability analysis. This is because the region of excited modes depends strongly on the radius of the star.

7 CONCLUSION

We have analysed two sources of photometric data for the fifth roAp star found in the *Kepler* satellite field-of-view. The multi-

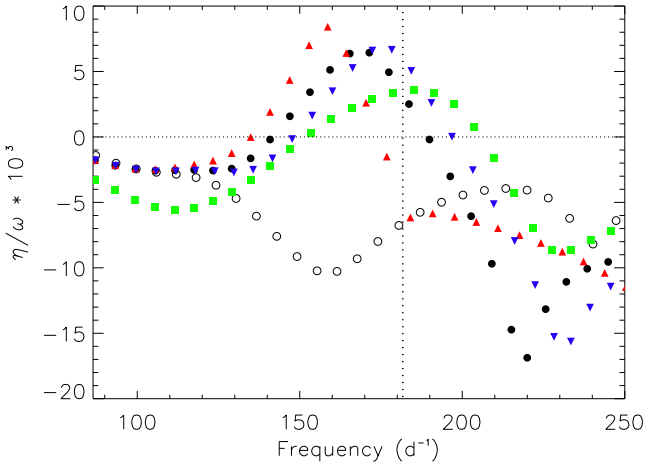

Figure 16. The relative growth rates for the four cases presented in Table 6. The black open circles are for the standard equatorial region (case A, equatorial) and the black filled circles for the standard polar region (case A, polar). The other three cases correspond to modifications to the standard polar region as described in the table: upwards red triangles for case B, down facing blue triangles for case C, and green squares for case D. The vertical dotted line represents the pulsation frequency. The oscillations are stable if the ratio between the imaginary, η, and the real, ω, parts of the eigenfrequencies is below zero.

Table 6. Modelling parameters for the cases illustrated in Fig. 16, all computed with $M = 1.8\,\mathrm{M}_{\odot}$, $T_{\rm eff} = 8000\,\mathrm{K}$, and $\log g = 4.18$.

Case	Model	$Y_{\rm surf}$	$\tau_{\rm min}$	Boundary condition
A	Equatorial	0.01	3.5×10^{-5}	Reflective
A	Polar	0.01	3.5×10^{-5}	Reflective
B	Polar	0.01	3.5×10^{-5}	Transmissive
C	Polar	0.1	3.5×10^{-5}	Reflective
D	Polar	0.01	3.5×10^{-4}	Reflective

season WASP data allow us to directly extract the pulsation frequency and amplitude of the star. Although the pulsations are above the Nyquist frequency of the *Kepler* LC data, we have also been able to reliably extract the pulsational multiplet frequencies, albeit at greatly diluted amplitudes.

Analysis of the pulsation frequencies has shown that the pulsation mode amplitude is stable, but the frequency is not, leading to "ragged" peaks when all data are combined to calculate a periodogram. One possibility for this mode instability is intrinsic variations in the pulsation cavity of the star, leading to slight variations in the frequency over many years.

Another model contributing to the frequency variability we have presented is that KIC 7582608 is a binary star. We have interpreted some of the frequency variations to be a result of Doppler shifts due to binary motion. Converting these shifts to radial velocities and applying a binary fitting code, we conclude that if the star is indeed in a binary, the orbit must be eccentric, with $e = 0.39$, and have a period of about 1200 d. This result may contradict the suggestion by Schöller et al. (2012) that magnetic Ap stars become roAp stars if they are not born in close binaries. Of course, the potential secondary object to KIC 7582608 may have been captured by the Ap star after formation. Further observations are planned for this star to increase the number of spectroscopic RVs to which a binary model can be fit.

Modelling of the pulsation frequency suggests that the pulsation in KIC 7582608 is driven by the κ-mechanism acting in the hydrogen ionisation zone, as is the case with most other roAp stars. The mode stability analysis produces results that are consistent with the effective temperature and luminosity of KIC 7582608 when convection is suppressed in the polar regions by the magnetic field.

ACKNOWLEDGEMENTS

DLH acknowledges financial support from the STFC via the Ph.D. studentship programme. MSC is supported by an Investigador FCT contract funded by FCT/MCTES (Portugal) and POPH/FSE (EC) and by funds from the ERC, under FP7/EC, through the project FP7-SPACE-2012-31284. The WASP project is funded and maintained by Queen's University Belfast, the Universities of Keele, St. Andrews and Leicester, the Open University, the Isaac Newton Group, the Instituto de Astrofisica Canarias, the South African Astronomical Observatory and by the STFC. We thank Luis Balona for providing roAp/noAp data for Fig. 2, and the referee, Hiromoto Shibahashi, for useful comments and suggestions.

REFERENCES

Asplund M., Grevesse N., Sauval A. J., Scott P., 2009, ARA&A, 47, 481
Balmforth N. J., Cunha M. S., Dolez N., Gough D. O., Vauclair S., 2001, MNRAS, 323, 362
Balona L. A., 2013, MNRAS, 436, 1415
Balona L. A. et al., 2011a, MNRAS, 413, 2651
—, 2011b, MNRAS, 410, 517
Bertelli G., Girardi L., Marigo P., Nasi E., 2008, A&A, 484, 815
Bevington P. R., 1969, Data reduction and error analysis for the physical sciences. New York: McGraw-Hill, 1969
Bigot L., Dziembowski W. A., 2002, A&A, 391, 235
Bigot L., Kurtz D. W., 2011, A&A, 536, A73
Cunha M. S., 2002, MNRAS, 333, 47
Cunha M. S., Alentiev D., Brandão I. M., Perraut K., 2013, MNRAS, 436, 1639
Droege T. F., Richmond M. W., Sallman M. P., Creager R. P., 2006, PASP, 118, 1666
Elkin V. G., Kurtz D. W., Mathys G., Freyhammer L. M., 2010, MNRAS, 404, L104
Elkin V. G., Kurtz D. W., Worters H. L., Mathys G., Smalley B., van Wyk F., Smith A. M. S., 2011, MNRAS, 411, 978
Everett M. E., Howell S. B., Kinemuchi K., 2012, PASP, 124, 316
Greiss S. et al., 2012, AJ, 144, 24
Holdsworth D. L. et al., 2014, MNRAS, 439, 2078
Kochukhov O., Alentiev D., Ryabchikova T., Boyko S., Cunha M., Tsymbal V., Weiss W., 2013, MNRAS, 431, 2808
Kurtz D. W., 1982, MNRAS, 200, 807
Kurtz D. W. et al., 2011, MNRAS, 414, 2550
Kurtz D. W., Martinez P., Koen C., Sullivan D. J., 1996, MNRAS, 281, 883
Kurtz D. W., Martinez P., van Wyk F., Marang F., Roberts G., 1994, MNRAS, 268, 641
Kurtz D. W., Shibahashi H., Goode P. R., 1990, MNRAS, 247, 558
Kurtz D. W., van Wyk F., Roberts G., Marang F., Handler G., Medupe R., Kilkenny D., 1997, MNRAS, 287, 69

Kurucz R., 1993, ATLAS9 Stellar Atmosphere Programs and 2 km/s grid. Kurucz CD-ROM No. 13. Cambridge, Mass.: Smithsonian Astrophysical Observatory, 1993., 13
Lenz P., Breger M., 2005, Communications in Asteroseismology, 146, 53
Martin D. C. et al., 2005, ApJ, 619, L1
Martinez P., Kurtz D. W., van Wyk F., 1994, MNRAS, 271, 305
Mathys G., 1990, A&A, 232, 151
Mathys G., Lanz T., 1992, A&A, 256, 169
Monet D. G. et al., 2003, AJ, 125, 984
Montgomery M. H., Odonoghue D., 1999, Delta Scuti Star Newsletter, 13, 28
Munari U., Zwitter T., 1997, A&A, 318, 269
Murphy S. J., Shibahashi H., Kurtz D. W., 2013, MNRAS, 430, 2986
Niemczura E. et al., 2014, in IAU Symposium, Vol. 301, IAU Symposium, Guzik J. A., Chaplin W. J., Handler G., Pigulski A., eds., pp. 467–468
Paxton B., Bildsten L., Dotter A., Herwig F., Lesaffre P., Timmes F., 2011, ApJS, 192, 3
Paxton B. et al., 2013, ApJS, 208, 4
Pollacco D. L. et al., 2006, PASP, 118, 1407
Press W. H., Rybicki G. B., 1989, ApJ, 338, 277
Press W. H., Teukolsky S. A., Vetterling W. T., Flannery B. P., 1992, Numerical recipes in FORTRAN. The art of scientific computing. Cambridge: University Press, —c1992, 2nd ed.
Schöller M., Correia S., Hubrig S., Kurtz D. W., 2012, A&A, 545, A38
Shibahashi H., Kurtz D. W., 2012, MNRAS, 422, 738
Skrutskie M. F. et al., 2006, AJ, 131, 1163
Smalley B., Smith K. C., Dworetsky M. M., 2001, UCLSYN Userguide, `http://www.astro.keele.ac.uk/~bs/uclsyn.pdf`
Smith A. M. S. et al., 2006, MNRAS, 373, 1151
Smith K. C., 1992, Ph.D. Thesis, University of London
Smith K. C., Dworetsky M. M., 1988, in Elemental Abundance Analyses, Adelman S. J., Lanz T., eds., p. 32
Southworth J., 2013, A&A, 557, A119
Tamuz O., Mazeh T., Zucker S., 2005, MNRAS, 356, 1466
Torres G., Andersen J., Giménez A., 2010, A&A Rev., 18, 67
Vogt S. S., 1987, PASP, 99, 1214

APPENDIX A: ADDITIONAL TABLES

Table A1. A linear least-squares fit of the quintuplet. For each Quarter, t_0 has been chosen to force the first sidelobes to have equal phase.

Quarter	ID	Frequency (d^{-1})	Amplitude (μmag)	Phase (rad)	Quarter	ID	Frequency (d^{-1})	Amplitude (μmag)	Phase (rad)
	$\nu - 2\nu_{\rm rot}$	181.6431	19.741 ± 2.485	1.659 ± 0.126		$\nu - 2\nu_{\rm rot}$	181.6268	14.607 ± 1.669	0.685 ± 0.114
	$\nu - \nu_{\rm rot}$	181.6910	40.390 ± 2.537	-1.269 ± 0.063		$\nu - \nu_{\rm rot}$	181.6758	38.438 ± 1.672	0.520 ± 0.044
Q01	ν	181.7390	123.843 ± 2.544	2.259 ± 0.021	Q10	ν	181.7247	113.928 ± 1.672	1.055 ± 0.015
	$\nu + \nu_{\rm rot}$	181.7870	36.489 ± 2.538	-1.342 ± 0.069		$\nu + \nu_{\rm rot}$	181.7737	35.002 ± 1.672	0.534 ± 0.048
	$\nu + 2\nu_{\rm rot}$	181.8349	11.999 ± 2.487	2.168 ± 0.207		$\nu + 2\nu_{\rm rot}$	181.8226	15.010 ± 1.669	0.674 ± 0.111
	$\nu - 2\nu_{\rm rot}$	181.6377	12.892 ± 1.812	-1.570 ± 0.141		$\nu - 2\nu_{\rm rot}$	181.6310	16.549 ± 1.558	2.799 ± 0.094
	$\nu - \nu_{\rm rot}$	181.6868	36.330 ± 1.818	-1.688 ± 0.050		$\nu - \nu_{\rm rot}$	181.6800	42.547 ± 1.559	-0.515 ± 0.037
Q02	ν	181.7358	117.870 ± 1.817	-1.040 ± 0.015	Q11	ν	181.7290	115.728 ± 1.561	-3.072 ± 0.014
	$\nu + \nu_{\rm rot}$	181.7849	44.590 ± 1.818	-1.666 ± 0.041		$\nu + \nu_{\rm rot}$	181.7781	40.892 ± 1.560	-0.497 ± 0.038
	$\nu + 2\nu_{\rm rot}$	181.8339	14.600 ± 1.812	-1.425 ± 0.124		$\nu + 2\nu_{\rm rot}$	181.8271	9.240 ± 1.559	2.828 ± 0.169
	$\nu - 2\nu_{\rm rot}$	181.6337	14.135 ± 1.520	2.753 ± 0.108		$\nu - 2\nu_{\rm rot}$	181.6344	15.754 ± 1.747	-1.083 ± 0.111
	$\nu - \nu_{\rm rot}$	181.6826	38.813 ± 1.519	-0.438 ± 0.039		$\nu - \nu_{\rm rot}$	181.6838	40.520 ± 1.746	-0.949 ± 0.043
Q03	ν	181.7316	122.950 ± 1.524	-3.075 ± 0.012	Q12	ν	181.7332	121.494 ± 1.748	-0.416 ± 0.014
	$\nu + \nu_{\rm rot}$	181.7805	43.710 ± 1.523	-0.432 ± 0.035		$\nu + \nu_{\rm rot}$	181.7826	43.475 ± 1.745	-0.917 ± 0.040
	$\nu + 2\nu_{\rm rot}$	181.8295	15.899 ± 1.520	2.878 ± 0.096		$\nu + 2\nu_{\rm rot}$	181.8319	13.826 ± 1.745	-0.673 ± 0.126
	$\nu - 2\nu_{\rm rot}$	181.6353	15.271 ± 1.533	-2.772 ± 0.100		$\nu - 2\nu_{\rm rot}$	181.6329	17.911 ± 1.550	2.217 ± 0.087
	$\nu - \nu_{\rm rot}$	181.6846	39.188 ± 1.536	0.172 ± 0.039		$\nu - \nu_{\rm rot}$	181.6817	41.099 ± 1.554	-0.946 ± 0.038
Q04	ν	181.7339	123.790 ± 1.534	-2.447 ± 0.012	Q13	ν	181.7306	125.120 ± 1.553	2.776 ± 0.012
	$\nu + \nu_{\rm rot}$	181.7832	45.875 ± 1.537	0.180 ± 0.033		$\nu + \nu_{\rm rot}$	181.7794	39.683 ± 1.553	-0.952 ± 0.039
	$\nu + 2\nu_{\rm rot}$	181.8324	17.410 ± 1.532	-2.740 ± 0.088		$\nu + 2\nu_{\rm rot}$	181.8282	11.574 ± 1.551	2.600 ± 0.134
	$\nu - 2\nu_{\rm rot}$	181.6312	14.139 ± 1.607	-2.986 ± 0.114		$\nu - 2\nu_{\rm rot}$	181.6369	17.362 ± 2.279	-0.798 ± 0.131
	$\nu - \nu_{\rm rot}$	181.6792	37.914 ± 1.616	-2.887 ± 0.043		$\nu - \nu_{\rm rot}$	181.6850	41.355 ± 2.298	-0.933 ± 0.056
Q05	ν	181.7272	117.505 ± 1.612	-2.419 ± 0.014	Q14	ν	181.7331	115.532 ± 2.306	-0.366 ± 0.020
	$\nu + \nu_{\rm rot}$	181.7752	36.364 ± 1.615	-2.907 ± 0.044		$\nu + \nu_{\rm rot}$	181.7812	41.746 ± 2.297	-0.940 ± 0.055
	$\nu + 2\nu_{\rm rot}$	181.8231	13.575 ± 1.607	-2.596 ± 0.119		$\nu + 2\nu_{\rm rot}$	181.8292	15.442 ± 2.279	-1.038 ± 0.148
	$\nu - 2\nu_{\rm rot}$	181.6312	9.305 ± 1.850	-3.064 ± 0.199		$\nu - 2\nu_{\rm rot}$	181.6331	16.573 ± 1.595	-1.985 ± 0.096
	$\nu - \nu_{\rm rot}$	181.6802	36.056 ± 1.854	-2.765 ± 0.051		$\nu - \nu_{\rm rot}$	181.6821	35.849 ± 1.601	-2.145 ± 0.045
Q06	ν	181.7292	113.495 ± 1.854	-2.212 ± 0.016	Q15	ν	181.7311	123.619 ± 1.604	-1.627 ± 0.013
	$\nu + \nu_{\rm rot}$	181.7782	41.683 ± 1.854	-2.762 ± 0.044		$\nu + \nu_{\rm rot}$	181.7802	43.531 ± 1.600	-2.152 ± 0.037
	$\nu + 2\nu_{\rm rot}$	181.8272	11.886 ± 1.850	-2.326 ± 0.157		$\nu + 2\nu_{\rm rot}$	181.8292	13.050 ± 1.594	-1.965 ± 0.122
	$\nu - 2\nu_{\rm rot}$	181.6301	14.240 ± 1.695	-0.707 ± 0.119		$\nu - 2\nu_{\rm rot}$	181.6383	18.673 ± 1.696	-2.639 ± 0.091
	$\nu - \nu_{\rm rot}$	181.6788	38.421 ± 1.697	-0.800 ± 0.044		$\nu - \nu_{\rm rot}$	181.6871	40.539 ± 1.717	0.308 ± 0.042
Q07	ν	181.7276	113.775 ± 1.699	-0.224 ± 0.015	Q16	ν	181.7359	121.373 ± 1.713	-2.267 ± 0.014
	$\nu + \nu_{\rm rot}$	181.7763	38.983 ± 1.697	-0.804 ± 0.044		$\nu + \nu_{\rm rot}$	181.7846	42.846 ± 1.716	0.309 ± 0.040
	$\nu + 2\nu_{\rm rot}$	181.8251	10.953 ± 1.696	-0.516 ± 0.155		$\nu + 2\nu_{\rm rot}$	181.8334	11.927 ± 1.697	-2.482 ± 0.142
	$\nu - 2\nu_{\rm rot}$	181.6291	14.525 ± 1.796	0.428 ± 0.124		$\nu - 2\nu_{\rm rot}$	181.6403	15.675 ± 2.683	1.605 ± 0.171
	$\nu - \nu_{\rm rot}$	181.6777	34.324 ± 1.797	0.455 ± 0.053		$\nu - \nu_{\rm rot}$	181.6880	40.562 ± 2.694	-1.123 ± 0.067
Q08	ν	181.7263	116.102 ± 1.803	0.998 ± 0.016	Q17	ν	181.7357	126.786 ± 2.709	2.686 ± 0.021
	$\nu + \nu_{\rm rot}$	181.7749	37.724 ± 1.799	0.459 ± 0.048		$\nu + \nu_{\rm rot}$	181.7835	42.579 ± 2.699	-1.102 ± 0.063
	$\nu + 2\nu_{\rm rot}$	181.8235	13.191 ± 1.797	0.657 ± 0.136		$\nu + 2\nu_{\rm rot}$	181.8312	14.389 ± 2.685	2.481 ± 0.186
	$\nu - 2\nu_{\rm rot}$	181.6230	12.911 ± 1.581	1.770 ± 0.123					
	$\nu - \nu_{\rm rot}$	181.6711	36.045 ± 1.588	1.652 ± 0.044					
Q09	ν	181.7191	112.235 ± 1.585	2.196 ± 0.014					
	$\nu + \nu_{\rm rot}$	181.7672	40.729 ± 1.587	1.635 ± 0.039					
	$\nu + 2\nu_{\rm rot}$	181.8153	11.504 ± 1.586	1.822 ± 0.137					

Table A2. Frequencies used to produce Fig. 14. The errors are calculated from a non-linear least-squares fit.

Time BJD	Frequency (d^{-1})	Time BJD	Frequency (d^{-1})
4963.7671	181.7320 ± 0.0008	5802.3528	181.7200 ± 0.0009
4984.2117	181.7345 ± 0.0008	5822.8063	181.7230 ± 0.0009
5168.2941	181.7279 ± 0.0007	5843.2594	181.7194 ± 0.0009
5188.7478	181.7301 ± 0.0008	5863.7128	181.7194 ± 0.0008
5209.2016	181.7288 ± 0.0008	5884.1660	181.7222 ± 0.0008
5229.6560	181.7281 ± 0.0008	5904.6193	181.7266 ± 0.0008
5250.1101	181.7283 ± 0.0007	5925.0727	181.7256 ± 0.0009
5270.5649	181.7276 ± 0.0009	5945.5263	181.7263 ± 0.0010
5291.0198	181.7257 ± 0.0008	5965.9804	181.7258 ± 0.0008
5311.4745	181.7235 ± 0.0008	5066.0280	181.7268 ± 0.0008
5331.9294	181.7206 ± 0.0008	5984.8715	181.7273 ± 0.0010
5352.3840	181.7190 ± 0.0009	6007.5842	181.7284 ± 0.0010
5004.4821	181.7343 ± 0.0008	6027.3340	181.7263 ± 0.0007
5372.8283	181.7197 ± 0.0008	6047.7788	181.7244 ± 0.0008
5393.2929	181.7226 ± 0.0010	6067.9677	181.7255 ± 0.0008
5413.7468	181.7235 ± 0.0009	6088.8822	181.7215 ± 0.0008
5434.2004	181.7265 ± 0.0009	6109.1427	181.7263 ± 0.0010
5454.6438	181.7241 ± 0.0010	6128.6775	181.7292 ± 0.0012
5475.0869	181.7220 ± 0.0008	6150.0715	181.7212 ± 0.0010
5495.5400	181.7229 ± 0.0008	6170.5048	181.7276 ± 0.0011
5516.0033	181.7210 ± 0.0008	5086.4811	181.7261 ± 0.0010
5536.4567	181.7200 ± 0.0008	6190.9585	181.7265 ± 0.0010
5549.6156	181.7340 ± 0.0063	6211.4119	181.7266 ± 0.0009
5026.0295	181.7310 ± 0.0010	6231.8650	181.7274 ± 0.0008
5577.9772	181.7216 ± 0.0008	6252.3183	181.7285 ± 0.0008
5597.8081	181.7205 ± 0.0007	6272.7716	181.7233 ± 0.0008
5618.2624	181.7197 ± 0.0008	6293.2248	181.7254 ± 0.0008
5638.7170	181.7165 ± 0.0008	6313.6787	181.7279 ± 0.0013
5659.1718	181.7133 ± 0.0009	6334.1328	181.7291 ± 0.0008
5679.6264	181.7131 ± 0.0009	6354.5869	181.7300 ± 0.0008
5700.0815	181.7132 ± 0.0009	6375.0414	181.7308 ± 0.0008
5720.5361	181.7140 ± 0.0009	5106.9345	181.7242 ± 0.0008
5740.9905	181.7181 ± 0.0008	6395.4963	181.7291 ± 0.0008
5761.4448	181.7162 ± 0.0010	6414.8678	181.7292 ± 0.0009
5045.5742	181.7295 ± 0.0007	5127.3876	181.7270 ± 0.0008
5781.8989	181.7176 ± 0.0008	5147.8410	181.7253 ± 0.0009

Table A3. Radial velocity measurements used to produce Fig. 15.

Time BJD	RV ($km\,s^{-1}$)	Orbital Phase	Time BJD	RV ($km\,s^{-1}$)	Orbital Phase
		WASP Measurements			
3198.0752	33.8740 ± 2.7464	0.0961	4316.4324	51.9240 ± 5.2791	0.0254
3209.0133	33.4756 ± 2.0667	0.1052	4634.0762	48.8651 ± 2.4607	0.2893
3209.0175	34.4544 ± 1.8562	0.1052	5004.5471	57.6739 ± 0.8293	0.5972
4263.6140	49.5729 ± 2.3153	0.9815	5370.0503	39.2848 ± 0.9058	0.9009
4283.0188	50.9015 ± 1.2920	0.9976			
		Kepler Measurements			
4969.5193	56.4493 ± 1.3612	0.5681	5705.8440	25.4675 ± 1.5437	0.1799
4988.8706	56.7084 ± 1.4855	0.5842	5726.2986	29.6631 ± 1.5466	0.1969
5011.7055	66.3719 ± 1.6475	0.6031	5746.7529	36.3605 ± 1.5402	0.2139
5030.8823	58.3534 ± 1.4691	0.6191	5767.2070	31.5044 ± 1.6158	0.2309
5051.3364	49.7120 ± 1.3093	0.6361	5787.6611	28.6040 ± 1.4977	0.2479
5071.7897	48.5287 ± 1.5284	0.6531	5808.1150	36.0218 ± 1.5763	0.2649
5092.2434	45.0591 ± 1.4496	0.6701	5828.5684	39.7112 ± 1.6092	0.2819
5112.6968	43.4423 ± 1.4387	0.6871	5849.0217	37.7732 ± 1.3943	0.2989
5133.1499	46.6247 ± 1.2990	0.7040	5869.4748	38.3586 ± 1.3958	0.3159
5153.6030	46.6250 ± 1.4314	0.7210	5889.9282	43.9849 ± 1.3632	0.3329
5173.1674	47.6350 ± 1.4521	0.7373	5910.3813	51.0960 ± 1.3936	0.3499
5195.0516	57.3907 ± 1.4170	0.7555	5930.8350	46.6841 ± 1.5171	0.3669
5214.9639	51.7571 ± 1.3571	0.7720	5951.2888	50.2033 ± 1.6614	0.3839
5235.4182	49.2860 ± 1.4313	0.7890	5971.7429	49.5742 ± 1.3861	0.4009
5255.8728	47.7015 ± 1.3118	0.8060	5992.1973	47.0606 ± 1.4947	0.4179
5276.3273	49.3531 ± 1.4662	0.8230	6012.6519	50.6747 ± 1.3699	0.4349
5296.7822	42.2438 ± 1.3001	0.8400	6033.1067	47.1976 ± 1.2533	0.4519
5317.2370	41.5897 ± 1.5476	0.8570	6053.5615	44.9607 ± 1.4562	0.4689
5337.6919	35.3159 ± 1.4623	0.8740	6074.0163	44.8032 ± 1.3711	0.4858
5358.1467	34.1897 ± 1.4421	0.8910	6094.4709	43.8970 ± 1.3106	0.5028
5378.6008	40.3191 ± 1.5196	0.9080	6113.5872	46.0190 ± 2.2752	0.5187
5399.0552	44.7721 ± 1.5833	0.9250	6137.5049	65.3551 ± 2.9457	0.5386
5419.4988	39.4650 ± 1.5712	0.9420	6155.8340	43.7882 ± 1.7461	0.5538
5439.9524	45.4938 ± 1.7445	0.9590	6176.2873	50.7768 ± 1.9439	0.5708
5460.4160	39.3453 ± 1.8627	0.9760	6196.7410	46.1893 ± 1.9796	0.5878
5480.8693	38.6341 ± 1.5015	0.9930	6217.1943	48.6851 ± 1.2788	0.6048
5501.3225	42.6083 ± 1.6560	0.0100	6236.6157	48.1910 ± 1.5989	0.6210
5521.7657	39.3860 ± 1.4660	0.0270	6259.9195	55.1713 ± 1.7476	0.6403
5542.2293	38.5864 ± 1.3828	0.0440	6278.5542	45.2504 ± 1.4912	0.6558
5562.6829	30.9665 ± 7.2416	0.0610	6299.0076	47.2231 ± 1.3649	0.6728
5583.1367	43.8159 ± 1.3629	0.0780	6319.4614	49.1835 ± 2.5602	0.6898
5603.5908	39.0943 ± 1.5518	0.0950	6339.9153	54.3449 ± 1.3614	0.7068
5624.0349	35.4591 ± 1.3780	0.1119	6360.3699	54.4262 ± 1.3964	0.7238
5644.4795	36.4433 ± 2.0544	0.1289	6380.7837	55.1782 ± 1.3183	0.7408
5664.9344	26.7362 ± 1.4514	0.1459	6401.8716	54.2052 ± 1.3573	0.7583
5685.3892	27.0453 ± 1.5588	0.1629	6417.7593	34.3778 ± 2.2375	0.7715
		Spectroscopic Measurements			
6132.8340	45.5689 ± 2.8384	0.5347	6471.7993	50.7300 ± 2.8384	0.8164